JACS
JOURNAL OF THE AMERICAN CHEMICAL SOCIETY
Article
pubs.acs.org/JACS

$CsSnI_3$: Semiconductor or Metal? High Electrical Conductivity and Strong Near-Infrared Photoluminescence from a Single Material. High Hole Mobility and Phase-Transitions

In Chung,[†] Jung-Hwan Song,[‡,⊥] Jino Im,[‡] John Androulakis,[†] Christos D. Malliakas,[†] Hao Li,[†] Arthur J. Freeman,[‡] John T. Kenney,[§] and Mercouri G. Kanatzidis*[,†]

[†]Department of Chemistry, Northwestern University, Evanston, Illinois 60208, United States
[‡]Department of Physics and Astronomy, Northwestern University, Evanston, Illinois 60208, United States
[§]OmniPV Inc., 1030 Hamilton Court, Menlo Park, California 94025, United States

Supporting Information

ABSTRACT: $CsSnI_3$ is an unusual perovskite that undergoes complex displacive and reconstructive phase transitions and exhibits near-infrared emission at room temperature. Experimental and theoretical studies of $CsSnI_3$ have been limited by the lack of detailed crystal structure characterization and chemical instability. Here we describe the synthesis of pure polymorphic crystals, the preparation of large crack-/bubble-free ingots, the refined single-crystal structures, and temperature-dependent charge transport and optical properties of $CsSnI_3$, coupled with *ab initio* first-principles density functional theory (DFT) calculations. *In situ* temperature-dependent single-crystal and synchrotron powder X-ray diffraction studies reveal the origin of polymorphous phase transitions of $CsSnI_3$. The black orthorhombic form of $CsSnI_3$ demonstrates one of the largest volumetric thermal expansion coefficients for inorganic solids. Electrical conductivity, Hall effect, and thermopower measurements on it show p-type metallic behavior with low carrier density, despite the optical band gap of 1.3 eV. Hall effect measurements of the black orthorhombic perovskite phase of $CsSnI_3$ indicate that it is a p-type direct band gap semiconductor with carrier concentration at room temperature of $\sim 10^{17}$ cm^{-3} and a hole mobility of ~585 cm^2 V^{-1} s^{-1}. The hole mobility is one of the highest observed among p-type semiconductors with comparable band gaps. Its powders exhibit a strong room-temperature near-IR emission spectrum at 950 nm. Remarkably, the values of the electrical conductivity and photoluminescence intensity increase with heat treatment. The DFT calculations show that the screened-exchange local density approximation-derived band gap agrees well with the experimentally measured band gap. Calculations of the formation energy of defects strongly suggest that the electrical and light emission properties possibly result from Sn defects in the crystal structure, which arise intrinsically. Thus, although stoichiometric $CsSnI_3$ is a semiconductor, the material is prone to intrinsic defects associated with Sn vacancies. This creates highly mobile holes which cause the materials to appear metallic.

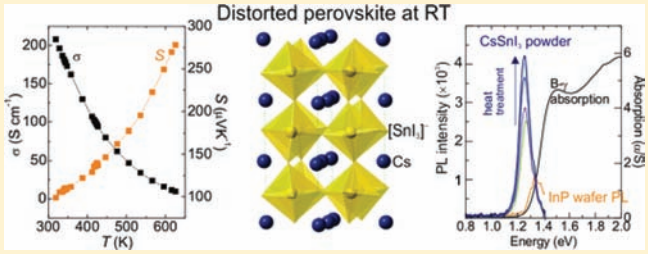

INTRODUCTION

$CsSnI_3$ is a unique phase-change material that exhibits four polymorphs.[1,2] Two polymorphs exist independently at room temperature: one has a one-dimensional double-chain structure and is yellow in color (Y), and another has a three-dimensional perovskite structure and is black in color (B-γ). When heated above 425K, the Y phase transforms to a black cubic perovskite phase (B-α), which, on subsequent cooling, converts to a black tetragonal phase (B-β) at 426 K (instead of Y) and a black orthorhombic phase (B-γ) at 351 K. This behavior was studied by X-ray powder diffraction (XRD) and differential thermal analysis (DTA).[1] The $CsSnI_3$ system is unique in combining two generally contra-indicated properties, strong photoluminescence (PL) and high electrical conductivity. Electrical conductivity of the black $CsSnI_3$ phase was measured and shown to be inversely proportional to temperature, indicating metallic behavior.[3] Thin films of $CsSnI_3$, deposited by a combination of thermal and e-beam evaporation methods, show a direct energy gap at 1.3 eV and an emission at 950 nm.[4]

Organic analogues of $CsSnI_3$ have been extensively studied. For example, a homologous series of $(C_4H_9NH_3)_2(CH_3NH_3)_{n-1}Sn_nI_{3n+1}$ compounds undergo a semiconducting (n < 3)-to-metallic (n > 5) transition with increasing n.[5] Its end member (n = ∞), cubic perovskite $CH_3NH_3SnI_3$ compound is claimed to be a low-carrier-density p-type metal.[5] The isostructural lead halide compounds $CH_3NH_3PbX_3$ (X = Br, I) efficiently sensitize TiO_2 for visible-light conversion to realize high voltages close to 1.0 V.[6] Theoretical calculations on $ASnX_3$ (A = Cs, CH_3NH_3, $NH_2CH{=}NH_2$; X = Cl, I) suggested that their electronic properties strongly depend on the structure of the inorganic

Received: February 16, 2012
Published: May 11, 2012

   dx.doi.org/10.1021/ja301539s | J. Am. Chem. Soc. 2012, 134, 8579−8587

Table 1. Crystallographic Refinement Details for four $CsSnI_3$ Polymorphs

	$CsSnI_3$			
code	B-α	B-β	B-γ	Y
color	black	black	black	yellow
temp/K	500	380	300	300
crystal system	cubic	tetragonal	orthorhombic	orthorhombic
space group	$Pm\bar{3}m$	$P4/mbm$	$Pnma$	$Pnma$
unit cell dimensions/Å	a = 6.2057(7)	a = 8.7182(8)	a = 8.6885(5)	a = 10.350(1)
		b = 8.7182(8)	b = 12.3775(4)	b = 4.7632(5)
		c = 6.1908(6)	c = 8.6384(6)	c = 17.684(2)
Z	1	2	4	4
V/Z, Å^3	238.99(5)	235.27(2)	232.25(2)	217.94(4)
d (calcd)/g cm^{-3}	4.393	4.463	4.521	4.818
crystal dimensions/mm^3		0.076 × 0.075 × 0.020		0.027 × 0.032 × 0.243
λ/Å	0.71073			
μ/mm^{-1}	16.018	16.271	16.482	17.565
F(000)	264	528	1056	1056
θ_{max}, deg	27.5	27.46	26.99	29.15
total/unique reflections	2004/81	3641/320	6924/1059	7977/1311
no. parameters	6	13	49	32
refinement method	full-matrix least-squares on F^2			
final R indices [$I > 2\sigma(I)$], $R_1{}^a/wR_2{}^b$	0.0289/0.0690	0.0656/0.01520	0.0431/0.0954	0.0288/0.0536
R indices (all data), R_1/wR_2	0.0345/0.0707	0.0822/0.1599	0.0553/0.0991	0.0421/0.0563
goodness-of-fit on F^2	1.171	1.128	1.192	1.049
largest diff peak and hole/e·A^{-3}	4.444/−1.483	2.091/−1.651	1.360/−1.709	0.731/−1.349

$^a R_1 = \sum||F_o| - |F_c||/\sum|F_o|$. $^b wR_2 = \{\sum[w(F_o^2 - F_c^2)^2]/\sum[w(F_o^2)^2]\}^{1/2}$.

cage and on the formation of the perovskite octahedral network.[7]

Despite its interesting physical and chemical properties, our understanding of the origin of such properties in $CsSnI_3$ is still limited. Additionally, many previous reports understate its high sensitivity to air, moisture, and organic solvents, resulting in an incorrect description of the phase change behavior and unreliable characterization results.[1,3] Some authors also revealed the inclusion of impurities in their syntheses.[2] Most importantly, the black phases of $CsSnI_3$ have never been structurally characterized because of the extreme difficulty of single-crystal X-ray diffraction (XRD) studies. As a result, theoretical and experimental studies have been severely limited, and the origin of its phase transition has never been understood.

Here we report the synthesis, single-crystal structure refinements, charge transport and optical properties, and theoretical calculation studies of all polymorphic forms of $CsSnI_3$. We determined the single-crystal structures of the three black polymorphs by *in situ* temperature-dependent single-crystal XRD studies for the first time. Examination of the coordination sphere of Cs^+ in the three perovskite frameworks suggests that the transitions are the result of the desire of the Cs^+ cation to achieve closest packing and the remarkable flexibility of the perovskite network thanks to the plasticity of the Sn−I−Sn angle. Based on an *in situ* temperature-dependent synchrotron powder XRD study, we probed in detail the reversible phase transitions. The interconversions of the four polymorphs proceed under specific conditions along with the influence of air, moisture, and organic solvents. Surprisingly, the black polymorphs exhibit one of the largest volumetric thermal coefficient for inorganic solid materials, close to that for liquid.

We also show with optical absorption spectroscopy, Hall effect, and Seebeck coefficient measurements that the black orthorhombic perovskite phase is a p-type direct band gap semiconductor with a band gap of 1.3 eV. We demonstrate that the $CsSnI_3$ is a unique system that combines two generally contra-indicated properties, strong PL and high electrical conductivity. The data show that the hole mobilities in this material are among the highest known in medium gap compound semiconductors (~585 cm^2 V^{-1} s^{-1}). Remarkably, its near-infrared PL emission at 950 nm is remarkably strong at room temperature and orders of magnitude greater than that of a standard commercially available InP single-crystalline wafer which also emits in the same wavelength. It is important to note that solid-state materials emitting near-IR light at room temperature are highly desirable for noninvasive investigations of paintings and artifacts,[8] optical amplifiers,[9] fiber-optic systems for telecommunications,[10] tunable solid-state laser systems, and biomedical applications.[11] Currently available materials for such applications are compounds containing lanthanides[12] and some III/V and II/VI semiconductors such as InP, GaAs, and CdTe. However, they show low emission efficiency. Therefore, materials that consist of environmentally friendly and inexpensive elements with high emission efficiency, such as $CsSnI_3$, are highly sought after.

Temperature-dependent electrical conductivity of the black phase shows metallic behavior, and, surprisingly, the conductivity and PL intensity gradually increase upon heat treatment. The results of *ab initio* density functional theory (DFT) calculations suggest that such phenomena may result from facile formation of Sn vacancies in the structure, which form hole carriers only in the black polymorphs of $CsSnI_3$.

EXPERIMENTAL SECTION

Synthesis. The synthesis of the pure black orthorhombic phase of $CsSnI_3$ was achieved by reacting a stoichiometric mixture of CsI and SnI_2 in an evacuated Pyrex tube at 550 °C for 1 h, followed by cooling for 6 h to room temperature. The synthesis of the pure yellow phase was achieved by reacting a stoichiometric mixture of CsI and SnI_2

dx.doi.org/10.1021/ja301539s | J. Am. Chem. Soc. 2012, 134, 8579−8587

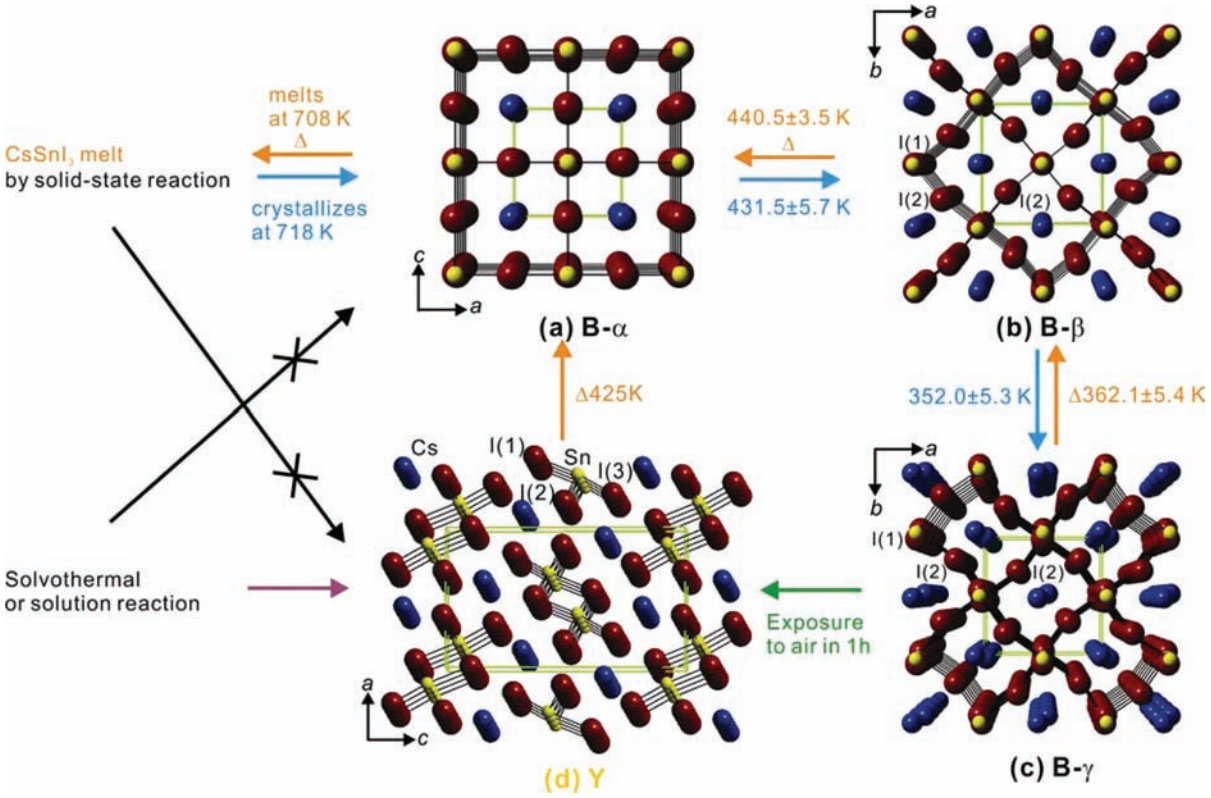

Figure 1. Illustration of phase change details of four $CsSnI_3$ polymorphs and their crystal structures. How phase transitions of $CsSnI_3$ polymorphs proceed is displayed with synthesis conditions and conversion temperatures obtained by *in situ* temperature-dependent synchrotron powder XRD studies. Crystal structures of the respective polymorph are shown: (a) black cubic (B-α) at 500 K; (b) tetragonal (B-β) at 380 K; (c) orthorhombic (B-γ) at 300 K; yellow (Y) phase at 300 K. Disordered atoms in (c) are omitted for clarity. Cs atoms, blue; Sn atoms, yellow; I atoms, violet. Green dashed lines represent a unit cell.

(total ~0.3 g) in ethylenediamine (0.2 mL) in an evacuated Pyrex tube at 140 °C for 3 d. Large crack- and bubble-free ingots (ca. 6 g) were prepared using a modified vertical Bridgman technique, and the growth condition was guided by the DTA results. Pure $CsSnI_3$ powder in an evacuated fused silica tube was passed down a single-zone Bridgeman furnace at a rate of 2 cm h^{-1}, maintained at 550 °C. The phase purity of the ingot obtained was confirmed by powder XRD analysis (Supporting Information, Figure S1).

Powder X-ray Diffraction. Powder XRD analysis was performed using a calibrated CPS 120 INEL powder X-ray diffractometer (Cu Kα graphite-monochromatized radiation) operating at 40 kV/20 mA and equipped with a position-sensitive detector with flat sample geometry.

***In Situ* Temperature-Dependent Synchrotron Powder X-ray Diffraction.** Fine powders of a black $CsSnI_3$ (B-γ) compound were sealed in an N_2-filled Roentgen glass tube. *In situ* synchrotron XRD (λ = 0.413975 Å) patterns were recorded from room temperature to 673 K at a rate of 5 K h^{-1} using at the 11-BM beamline at the Advanced Photon Source.

Single-Crystal X-ray Crystallography. Intensity data for black and yellow $CsSnI_3$ were collected at 300(2)−500(2) K on a STOE IPDS 2T diffractometer with Mo Kα radiation operating at 50 kV and 40 mA with a 34 cm diameter imaging plate under N_2 atmosphere. Individual frames were collected with a 3 min exposure time and a 1.0ω rotation. The X-AREA, X-RED, and X-SHAPE software packages were used for data extraction and integration and to apply empirical and analytical absorption corrections. The SHELXTL software package[13] was used to solve and refine the structure. The parameters for data collection and the details of the structural refinement are given in Table 1. Fractional atomic coordinates and displacement parameters are given in Supporting Information, Tables S1−S8. The selected bond distances and angles are given in Tables S9 and S10.

Charge Transport and Thermopower Measurements. The ingot was cut and polished into a rectangular shape with dimensions of ~2 mm × 3 mm × 8 mm under N_2 atmosphere. Electrical conductivity and Seebeck coefficient were measured simultaneously under He atmosphere from room temperature to 650 K on a ULVAC-RIKO ZEM-3 instrument system. The mechanical electrodes made of Rh/Pt and Pt were directly contacted to the ingot with no use of a chemical paste. Six heating and cooling cycles were repeated for a given sample.

Hall Effect Measurements. The Hall coefficient was measured on a polycrystalline bar-shaped ingot with four cold-pressed In contacts (one on each side of the ingot) positioned in a standard Hall geometry. The sample was subjected to a flow of nitrogen gas to protect it from oxidation during measurements. A dc current source (6220 Keithley Instruments) was utilized to supply a constant 100 mA current through the sample, while an external magnetic field up to ±1.4 T was applied in steps of 0.25 T. The voltage response, in both the positive and negative directions of the magnetic field, was recorded at each respective step by a nanovoltmeter (2182A Keithley Instruments), and half the difference of the two signals was recorded as the Hall voltage.

Optical Absorption Spectroscopy. Optical diffuse reflectance measurements were performed at room temperature using a Shimadzu UV-3101 PC spectrometer operating in the 200−2500 nm region. The reflectance versus wavelength data generated were used to estimate the band gap of the material by converting reflectance to absorption data according to the Kubelka−Munk equation: $\alpha/S = (1 - R)^2(2R)^{-1}$, where R is the reflectance and α and S are the absorption and scattering coefficients, respectively. The details of the energy gap measurements have been discussed elsewhere.[14]

Theoretical Calculations and Electronic Structures. The electronic structures of $CsSnI_3$ were calculated by the full potential linearized augmented planewave (FLAPW) method[15] based on DFT; experimental lattice constants and atomic coordinates were employed. The muffin-tin radii for Cs, Sn, and I atoms were chosen to be 2.90, 2.70, and 2.50 Bohr, respectively. The cutoff energies for the

dx.doi.org/10.1021/ja301539s | J. Am. Chem. Soc. 2012, 134, 8579−8587

planewave basis and star function were 13 and 144 Ry, respectively; 5×5×3 and 5×9×3 meshes of special *k*-points were used in the irreducible Brillouin zone for the B-γ and Y phases, respectively. Within the local density approximation (LDA), the Hedin–Lundqvist form[16] of the exchange-correlation functional was used, and spin–orbit coupling (SOC) was included by a second variation method.[17] In order to improve the accuracy of the band gap, which is usually underestimated within LDA, the nonlocal scheme of the screened-exchange LDA (sX-LDA) method was also employed.[18] This method leads to good agreement with experimentally measured band gaps and improves the conduction band topology as well.[14,19]

Defect Formation Energy Calculations. The defect formation energy is a function of the chemical potentials of atoms and electron. The set of chemical potentials is determined by the experimental growth condition. Based on the total energy from the *ab initio* calculation, we calculate the defect formation energy, $\Delta H_{D,q}$,[20] defined by the eq 1:

$$\Delta H_{D,q} = [E_{D,q} - E_H] + q(\Delta E_F + E_v) + \sum n_\alpha(\mu_\alpha^0 + \Delta\mu_\alpha) \quad (1)$$

In this formula, the first term on the right-hand side defines the binding energy ΔE of the defect D in the host system. The second term represents the energy of the charge q change from the Fermi level $E_F = \Delta E_F + E_v$, where E_v is the energy of the valence band maximum of host system. The third term is the energies of atoms of species α added to (or removed from) reservoirs of elements with chemical potential $n_\alpha = \mu_\alpha^0 + \Delta\mu_\alpha$, where μ_α^0 is the reference energy of the most stable phase of each element. Possible ranges of $\Delta\mu_\alpha$ are determined by the thermodynamic stable condition of host material, and ΔE_F is obtained as a function of temperature within the charge neutrality condition. To reduce the effect caused by finite cell size, we considered a large supercell which includes 360 atoms. For each defect, the internal coordinates of atoms are relaxed. Relaxation and total energy of pristine and each defected supercell are calculated by using a plane wave basis and projector augmented wave method[21] which is implemented in the Vienna *ab initio* simulation package.[22] The energy cutoff for the plane wave basis set was set to 300 eV. For the *k*-point sampling, a 1×1×1 mesh is used in the relaxation, and a 3×3×3 mesh is used for total energy calculations. The generalized gradient approximation (GGA) is used for the exchange-correlation functional within the Perdew–Burke–Ernzerhof (PBE) formalism;[23] the SOC interaction is not considered here.

RESULTS AND DISCUSSION

Synthesis, Crystal Structure, and Phase Transitions. The yellow phase of $CsSnI_3$ was isolated and structurally characterized in 1980,[24] whereas the black phases were only studied by powder XRD two decades ago.[1] We observed that obtaining suitable single crystals for XRD analysis of black phases is extremely difficult. When melts of $CsSnI_3$ cool to form crystals, a phase transition typically occurs anisotropically from higher to lower symmetry, resulting in inhomogeneous crystallographic domains in the crystals. Starting materials of CsI and SnI_2 that contain even very minor impurities give mixtures of the Y and B-γ phases in solid-state reactions, with single crystals of only the Y phase. When exposed to air, the B-γ crystals promptly lose single crystallinity, rapidly transform to the polycrystalline yellow phase, and ultimately decompose.

We determined the single-crystal structures of the three metastable black polymorphs for the first time (Table 1). To obtain the high-temperature B-α phase, a melt of $CsSnI_3$ was quenched at 623 K. The lustrous black block-like crystal was immediately sliced to a thin plate to minimize stress by the phase transitions and loaded on a single-crystal diffractometer, maintained at 500 K. The single crystal chosen showed a single crystallographic domain, indexed to a cubic unit cell. The B-α phase forms in the ideal three-dimensional perovskite structure with cubic $Pm\bar{3}m$ space group (Figure 1a). All Cs, Sn, and I atoms reside on the special positions of the space group. The Sn^{2+} center sits in an ideal octahedral geometry with six I^- anions, resulting in stereochemically inactive $6s^2$ lone pair electrons. The more common coordination geometries for Sn^{2+} are trigonal pyramidal found in $SnCl_2$ and SnS and square pyramidal found in SnO and α-$SnWO_3$. The $[SnI_{6/2}]^-$ octahedra condense to form a three-dimensional cubic framework via corner-sharing with the Cs^+ countercations residing at 12-coordinate interstices within the network made by eight $[SnI_{6/2}]^-$ octahedra. The Sn–I distance is normal at 3.1028(4) Å, and the bond angle of I_{ap}–Sn–I_{eq} is 90°.

When cooled, the cubic form undergoes successive displacive phase transitions to lower symmetry with no bond breaking (Figure 1b,c). The $Pm\bar{3}m$ symmetry is lowered to tetragonal $P4/mbm$ at 380 K (B-β) and orthorhombic *Pnma* at 300 K (B-γ). The B-β phase results from the tilting of the neighboring $[SnI_{6/2}]^-$ octahedra in only the *ab* plane to give Sn–$I(2)_{eq}$–Sn = 167.989° (Glazer tilting system: $a^0a^0c^-$) (Figure S2). The Sn–I distances slightly differ: Sn–$I(1)_{ap}$, 3.0954(3) Å; Sn–$I(2)_{eq}$, 3.0994(5) Å. Neither tilting of the octahedra viewed down the *c* axis nor the bent bond angle in the $[SnI_{6/2}]^-$ octahedron is observed: Sn–$I(1)_{ap}$–Sn, 180°; $I(2)_{eq}$–Sn–$I(2)_{eq}$, 90°; $I(1)_{ap}$–Sn–$I(2)_{eq}$, 90°. The new cell is enlarged to a $\sqrt{2}a\times\sqrt{2}a\times a$ supercell with $Z = 2$ (Z is the number of formula units per unit cell). In the B-γ phase at room temperature, octahedral tilting occurs along both the apical and equatorial directions ($a^+a^-a^-$) to give bond angles of 157.6(4)° and 166.0(3)° for Sn–$I(1a)_{ap}$–Sn and Sn–$I(2a)_{eq}$–Sn, respectively (Figure S1). Some internal bond angles of the $[SnI_{6/2}]^-$ octahedron are also slightly distorted to give the $I(1a)_{eq}$–Sn–$I(2a)_{eq}$, 88.6(2)° and 88.9(1)°, and *cis*-$I(2a)_{ap}$–Sn–$I(2a)_{eq}$, 89.95(3)°, while those of $I(1a)_{ap}$–Sn–$I(1a)_{ap}$ and the *trans*-$I(2a)_{eq}$–Sn–$I(2a)_{eq}$ remain at 180°. The distances of Sn–$I(1a)_{ap}$ and Sn–$I(2a)_{eq}$ deviate more than those in the B-β phase: 3.124(5) and 3.118(1) Å, respectively. Consequently, the $\sqrt{2}a\times2a\times\sqrt{2}a$ supercell is obtained with $Z = 4$. Note that investigation of the reciprocal lattice using the extended X-ray exposure did not reveal any superstructure or twinning.

When exposed to air or organic solvents such as acetonitrile, the B-γ phase undergoes a significant reconstructive phase transition to the Y phase at room temperature in 1 h (Figure 1d). The composition of the latter is better described as $Cs_2Sn_2I_6$. The edge-sharing $[SnII_{2/2}I_{3/3}]^-$ octahedra condense to form infinite one-dimensional double chains of $^1_\infty[Sn_2I_6^{2-}]$ running down the crystallographic *b* axis, separated by Cs^+ cations. There is one crystallographically independent Sn and Cs atom and three I atoms. The $[SnI_{6/2}]^-$ octahedra are distorted to give I–Sn–I angles ranging from 91.28(2)° to 96.32(2)°. The Sn–I distances are 3.2243(6) and 3.1968(6) Å to bridging I(1) and (2) atoms, respectively, and 2.9518(8) Å to the terminal I(3) atom. It is important to note that the B-γ phase does not spontaneously transform to the Y phase under an inert atmosphere. Some previous reports incorrectly indicated that grinding the black phase gave the yellow polymorph.[1] Such a transition results from exposure to air, not pressure. The Y phase transforms to the B-α phase on heating above 425 K under inert atmosphere.

Local Coordination Environment. Examination of the coordination environment and anisotropic displacement parameters (ADPs) of Cs atoms obtained from single-crystal XRD studies provided important clues on what drives these phase transitions (Tables S5–S8). At 500 K, the Cs atoms

dx.doi.org/10.1021/ja301539s | J. Am. Chem. Soc. 2012, 134, 8579–8587

reside in the ideal, 12-coordinated cuboctahedral geometry with a Cs–I distance of 4.3881(5) Å. Note that this distance is significantly longer than that found in CsI (3.94 Å) and the sum of the ionic radii of I^- and 12-coordinated Cs^+ (4.08 Å).[25] The ADPs of Cs atoms at this elevated temperature are unusually high: $U_{11} = U_{22} = U_{33} = 0.154$ Å^2; $U_{23} = U_{13} = U_{12} = 0$ Å^2, but are isotropic by symmetry. These data indicated that the Cs atoms randomly rattle inside the oversized perovskite cages, as observed in clathrate compounds (Figure 2a). The ADPs of I

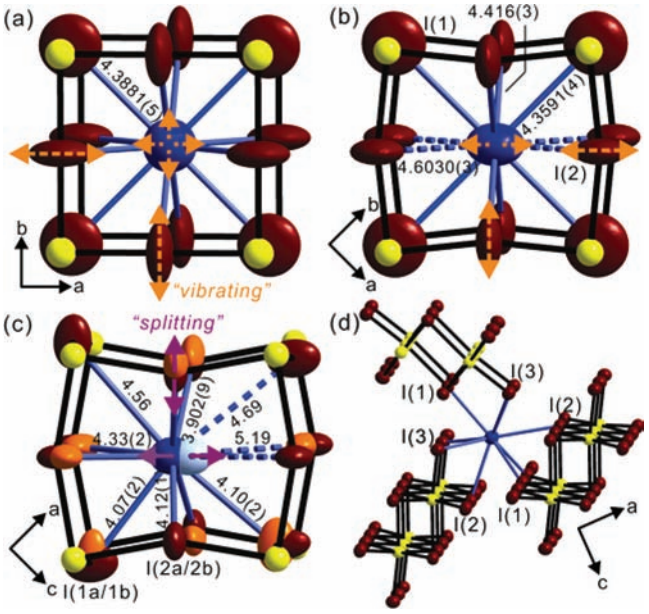

Figure 2. Coordination environments of Cs atoms in the $^3_\infty[SnI_3^-]$ perovskite cage in the black phases at (a) 500 K (B-α), (b) 380 K (B-β), and (c) 300K (B-γ). (d) Cs atoms are surrounded by three $^1_\infty[Sn_2I_6^{2-}]$ chains in the yellow phase (Y). Split models of I and Cs atoms are shown in (c). I atoms are labeled. Cs atoms, blue; Sn atoms, yellow; I atoms, wine in (a), (b), and (d). In (c), Cs(a) atoms, blue; Cs(b), light blue; Sn atoms, yellow; I(1a,2a) atoms, wine; I(1b,2b) atoms, orange. The Cs–I bond distances are given in Å. The thermal ellipsoids are shown at 80% probability.

atoms indicate large thermal vibrations perpendicular to the Sn–I–Sn bonds: $U_{11} = 40(1)$, $U_{22} = U_{33} = 0.215(2)$ Å^2; $U_{23} = U_{13} = U_{12} = 0$ Å^2. Correspondingly, the Sn–I–Sn bonds are flexible and can bend in order to distort the cages and get Cs and I atoms closer.

When cooled to 380 K, the $^3_\infty[SnI_3^-]$ framework compress slightly along the *ab* axis to make the Sn–I(1)$_{ap}$–Sn angles bend, but still with high ADPs in the I atoms (Figure 2b). Cs atoms vibrate ellipsoidally ($U_{11} = U_{22} = 0.134(3)$ Å^2, $U_{33} = 0.120(4)$ Å^2) along the elongated direction (*a* and *b* axes) of the cages. The Cs atoms sit in a distorted cuboctahedral geometry, and, because of this distortion, four of the Cs–I bonds become significantly shorter than those at 500 K: four each of 4.146(3), 4.3591(4), and 4.6030(3) Å (Table S10).

At room temperature, Cs and I atoms finally have to be modeled with split positions and their occupancies refined (Figure 2c). As a result, the ADPs of Cs and I atoms are close to normal. The occupancy ratios of Cs(a):Cs(b), I(1a):I(1b), and I(2a):I(2b) were refined to 76:24, 75:25, and 77:23, respectively. The Cs(a) atom shifts to one side of the distorted cage to effectively interact with I atoms, as does the Cs(b) atom in the opposite direction. As a result, nine of the Cs(a)–I distances, including the shortest of 3.902(9) Å, become significantly shorter than that at 500 K of 4.3881(5) Å. The longer distances to the opposite side of the shifted Cs(a) atoms are as long as 5.19 Å, where Cs(b) occupies the void.

Cs atoms in the yellow phase no longer rattle in the oversized cages but instead are eventually stabilized in a nine-coordinated tricapped trigonal prism geometry, surrounded by three adjacent $^1_\infty[Sn_2I_6^{2-}]$ chains. The Cs–I distances narrowly range from 3.8760(7) to 4.0687(9) Å, much shorter than those of the black phases, and the APDs of all atoms are nearly ideal.

The cell volume per formula unit decreases throughout the phase transitions from cubic perovskite to yellow phases: B-α, 239.99(5) Å^3; B-β, 235.27(2) Å^3; B-γ, 232.25(2) Å^3; Y, 217.94(4) Å^3 (Table 1 and Figure S4). The mass density calculated from the structural models presented above increases from B-α, 4.393 g cm^{-3}; B-β, 4.463 g cm^{-3}; B-γ, 4.521 g cm^{-3}; to Y, 4.818 g cm^{-3}. It is also interesting to note that the phase change between the two room-temperature forms involves a remarkable 6.6% increase in density. Thus, the yellow phase is the best packing model for the $CsSnI_3$ stoichiometry and likely the thermodynamically stable form.

To confirm our assumption that stabilization of Cs atoms in $CsSnI_3$ plays a key role in phase transitions, we examined relevant phases that include different size combinations of component atoms. Presumably due to the smaller size of Rb, the perovskite phase of $RbSnI_3$ does not exist (the cage for the Rb atoms is too large) and instead only forms the one-dimensional structure isomeric to yellow $CsSnI_3$.[3,26] In contrast, the bigger, asymmetric $CH_3NH_3^+$ cation can better support the cages and only forms a cubic perovskite with no phase transition near room temperature.[27] Indeed, $[CH_3NH_3]SnI_3$ shows even larger cell volume per formula unit of 243.4(1) Å^3 than black $CsSnI_3$ at room temperature.[27] With a smaller cage of $^3_\infty[SnBr_3^-]$, $CsSnBr_3$ can only form the perovskite structure.[2]

***In Situ* Temperature-Dependent Synchrotron X-ray Diffraction.** To track each phase transition, we performed *in situ* temperature-dependent synchrotron powder XRD studies on the B-γ phase from room temperature to 673 K. Figure 3 shows the temperature dependence of XRD patterns on heating at a rate of 5 K h^{-1} with a 2θ range of 5.3–6.9° for selective temperatures. The XRD pattern at room temperature confirmed the purity of the B-γ phase. The doublet around

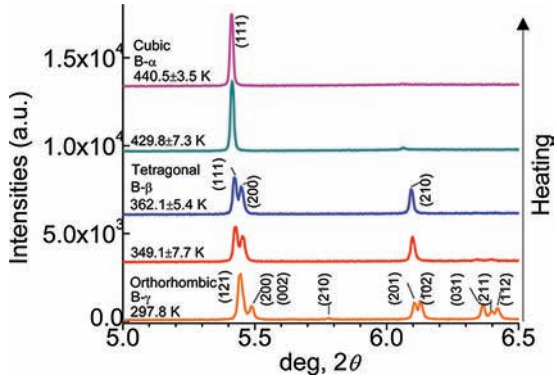

Figure 3. *In situ* temperature-dependent synchrotron XRD patterns of black $CsSnI_3$ on heating. Changes in the Bragg reflection peaks indicate temperature-driven phase transitions to higher symmetry on heating: orthorhombic (B-γ) to tetragonal (B-β) above 362.1 ± 5.4 K and the latter to orthorhombic (B-α) above 440.5 ± 3.5 K. The representative XRD peaks that reflect phase transitions are indexed.

dx.doi.org/10.1021/ja301539s | J. Am. Chem. Soc. 2012, 134, 8579–8587

6.11−6.13° (indexed as the (201) and (102) reflections) starts merging into a single peak at 6.09° (indexed as the (210) reflection of the tetragonal cell) above 338.0 ± 3.4 K. Above 372.1 ± 4.6 K, the characteristic Bragg peaks of the orthorhombic cell completely disappear: (210), (031), (211), and (112), indicative of forming the tetragonal B-β phase. On subsequent heating, the (200) and (210) peaks vanish, indicating the formation of the cubic B-α phase above 440.5 ± 3.5 K, which is stable up to 673.0 K. On cooling, the opposite trend is observed. At 420.1 ± 5.8 K, the (200) and (210) peaks evolve to restore the B-β form. Below 352.0 ± 5.3 K, the Bragg peaks of the B-γ phase start to appear (Figure S3). The results confirm the reversibility of the phase transition among the black phases.

The cell volume changes smoothly as a function of temperature with no noticeable discontinuity by the phase transition (Figure S4). For the black phase, the coefficients of the linear thermal expansion are $\alpha_a = 5.01 \times 10^{-5}$ K^{-1}, $\alpha_b = 1.42 \times 10^{-5}$ K^{-1}, and $\alpha_c = 7.71 \times 10^{-4}$ K^{-1}. The coefficient of the volumetric thermal expansion at 298 K is measured to be $\beta = 1.26 \times 10^{-4}$ K^{-1}. This value is unusually large for solid and close to that for liquid. For example, those for PbTe, Hg, and distilled water at 293 K are 0.2×10^{-4}, 1.82×10^{-4}, and 2.07×10^{-4} K^{-1}, respectively. Since the observed value is one of the largest for solid-state inorganic materials, we present theoretical calculations of bulk modulus below in the Electronic Structure Calculation section to explain these observations.

Figure 1 illustrates the phase transition details of the four polymorphs. The transition between the black phases is reversible, driven by temperature under inert atmosphere, as shown by *in situ* synchrotron XRD studies. The transition from the B-γ to the Y phase, typically activated by exposure to air, moisture, or organic solvents, readily proceeds at room temperature, whereas the reverse requires heating above 425 K. Under inert conditions, the B-γ phase, however, is stable for more than a year. The black phase congruently melts at 708 K and recrystallizes at 718 K (measured at the onset, Figure S5). It should be noted that the pure black phase is obtained only by solid-state reaction, whereas the pure yellow phase is prepared only by solution or solvothermal reactions. Several authors incorrectly reported a compound greenish in color. The greenish color is typically the Y phase contaminated by the B-γ and/or Cs_2SnI_6[28] that includes Sn^{IV}. Cs_2SnI_6 is also a typical impurity in the solution synthesis of the Y phase and is black in color.

Charge Transport Properties. For the charge transport property measurements, we prepared large, crack-free polycrystalline ingots (ca. 8 g). Our crystal growth conditions were guided by the DTA results. Sample preparation and all measurements were carried out under inert atmosphere. Mechanical contacts made of Pt/Rh and Pt were directly applied to the rectangular ingot with no application of a paste that typically contains organic solvents. The temperature dependence of the electrical conductivity and the Seebeck coefficient over six independent heating cycles at a rate of 5 K h^{-1} between individual steps show highly unusual behavior (Figure 4). Although the electrical conductivity decreases with increasing temperature over the entire temperature range, indicating metallic behavior, with each heating cycle the overall conductivity rises.

Because of the rise in electrical conductivity after each heating cycle, we attempted to determine if the increase was permanent. One week after measuring four cycles, we performed a second run on the same ingot. The electrical conductivity at room temperature shows a value similar to that obtained for the fourth cycle, indicating that the increased value of the electrical conductivity is sustained. Over the course of six heating cycles, conductivity rises drastically from 16 to 208 S cm^{-1} at room temperature. Therefore, heat energy boosts the carrier concentration.

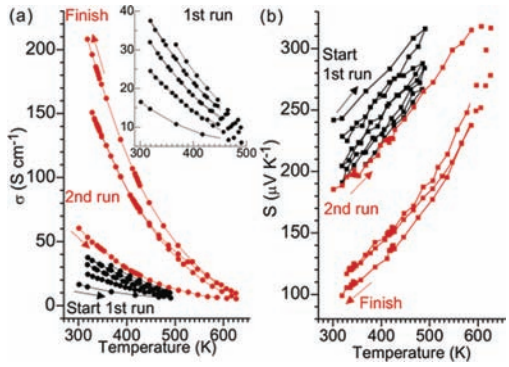

Figure 4. (a) Temperature-dependent electrical conductivity. The first run (●) is enlarged in the inset for clarity. (b) Seebeck coefficients of black $CsSnI_3$ in (a). In both plots the second run (■) was performed 1 week after the first run.

Thermoelectric power measurements gave positive Seebeck coefficients, suggesting p-type conduction, which increase with increasing temperature. Their values steadily decrease through all the heating cycles, consistent with the increase in the electrical conductivity. The value at room temperature dramatically diminishes from 242 to 99 μV K^{-1} over these measurements. Hall effect measurements of the pristine material show a low carrier concentration at room temperature of $p < 10^{17}$ cm^{-3}, indicative of p-type conduction and consistent with the positive Seebeck coefficient. The calculated resistivity and mobility are 0.9 Ω cm and 585 cm^2 V^{-1} s^{-1}, respectively, and are comparable to those obtained from transport property measurements: ρ = 1 Ω cm and μ = 400 cm^2 V^{-1} s^{-1}. This mobility is one of the highest observed among p-type semiconductors with comparable band gaps. In comparison, GaAs (E_g = 1.45 eV) and InP (E_g = 1.3 eV) exhibit hole mobility of 400 and 700 cm^2 V^{-1} s^{-1} at room temperature, respectively.[29] Discontinuities arising from the phase transition are not observed in the electrical conductivity or thermopower measurements, consistent with the result from synchrotron XRD studies (Figures S3 and S4).

Optical Properties. The two distinct polymorphic forms at room temperature (B-γ and Y) display a striking contrast in optical band gaps because of the significant structural differences. Optical absorption spectra reveal sharp absorption edges at 1.3 eV for the B-γ and 2.55 eV for the Y phases (Figure 5). A discussion on what causes the optical contrast is given below in the *ab initio* theoretical calculations section. When excited with 533 nm light irradiation at room temperature, the B-γ phase exhibits strong near-IR PL at ca. 950 nm. The PL intensity of as-prepared powders is several times larger than that of a single-crystalline InP wafer (Figure 5). Materials exhibiting strong near-IR emission operating at room temperature are rare and highly desirable. For example, emission at 950 nm is preferred for biomedical analysis because IR light better penetrates human tissues than UV and visible lights to give higher resolution images, and wavelengths between 700 and 950 nm are least absorbed by the tissues.[30] Such an

dx.doi.org/10.1021/ja301539s | J. Am. Chem. Soc. 2012, 134, 8579−8587

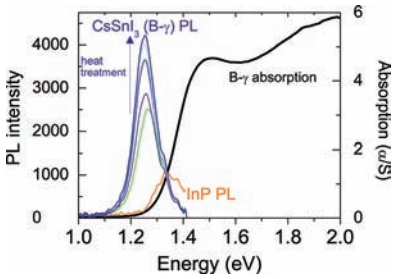

Figure 5. Optical absorption and photoluminescence spectra of black $CsSnI_3$ (B-γ) at room temperature. PL ($\lambda_{max} \approx 950$ nm) and optical absorption spectra of the B-γ phase showing a band edge at 1.3 eV are displayed. PL intensity steadily increases over heat treatment, which is compared with that of a single-crystalline InP wafer.

emission is also highly desirable for current silica-based telecommunication systems having standard telecommunication windows at 980 nm.[9]

We examined the optical emission and absorption spectra as well as the powder XRD patterns after the same heat treatment cycles employed in the charge transport property measurements. Surprisingly, the PL intensities gradually increased after each cycle, similar to the trend in the electrical conductivity. However, no noticeable changes in the optical absorption edges and XRD patterns were observed, indicating no structural change or deformation in the compound.

Electronic Structure Calculations. To understand the nature of the band gaps of the black and yellow phases and their striking difference in properties, we performed *ab initio* DFT calculations using the FLAPW method.[15] Experimental lattice constants and atomic coordinates were employed. Within the LDA, the Hedin–Lundqvist form[16] of the exchange-correlation functional was used, and SOC was

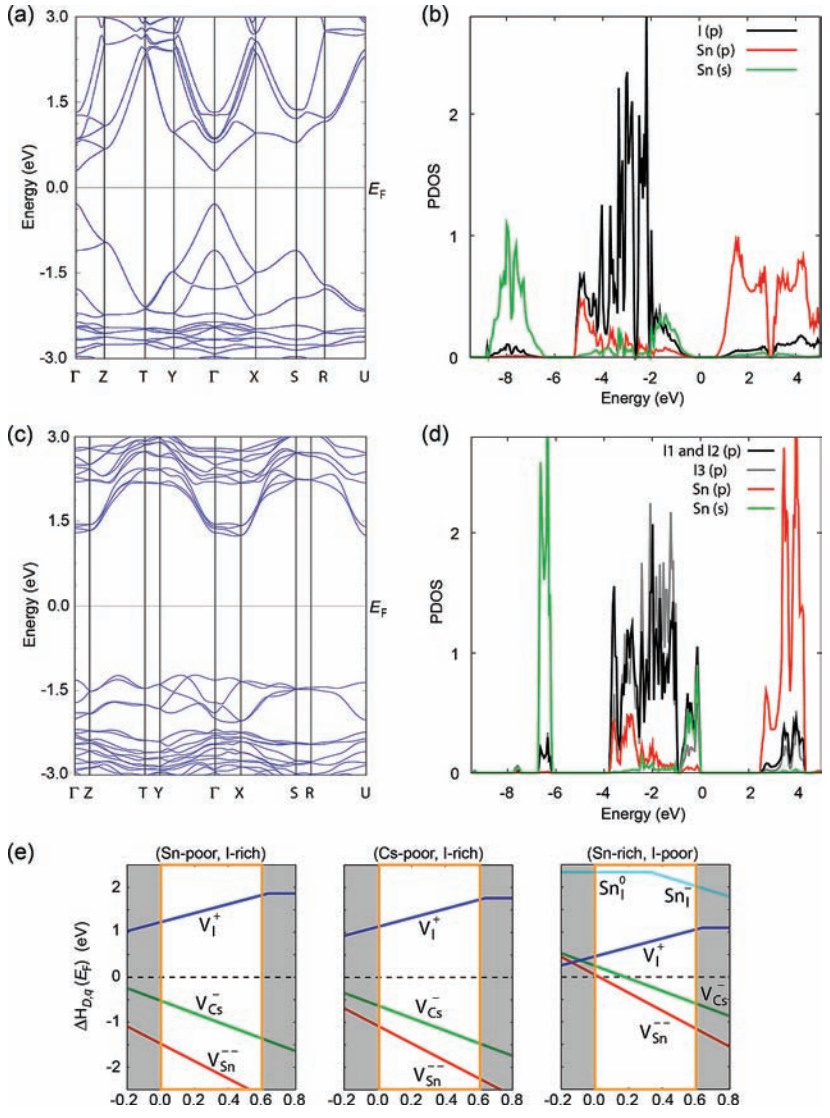

Figure 6. Calculated band structures of (a) the B-γ and (c) Y phase using the sX-LDA method, showing the direct and indirect band gap nature, respectively. The projected density of states (PDOS) for individual atoms calculated with the sX-LDA method for (b) the B-γ and (d) Y phases is shown. (e) Diagrams of calculated defect formation energies for V_{Sn}, V_{Cs}, Sn_I, and V_I in the B-γ form. Charge state, q, is denoted by +, 0, and −. The energy level of the VBM is set to zero. The regions below VBM and above CBM are shaded in gray color. The defect formation energies of Sn_I are higher than 2.5 eV in the Sn-poor, I-rich and the Cs-poor, I-rich conditions.

dx.doi.org/10.1021/ja301539s | J. Am. Chem. Soc. 2012, 134, 8579–8587

included by a second variation method.[17] In order to improve the accuracy of the band gap, which is usually underestimated within LDA, the nonlocal scheme of the sX-LDA method was also employed.[18] This method leads to good agreement with the experimentally measured band gaps and improves the conduction band topology as well.[14,19]

The band structure and projected density of states (PDOS) for orthorhombic black $CsSnI_3$ (B-γ) are presented in Figure 6a,b. The band structure calculated by the sX-LDA method with SOC determines a direct band gap between the valence band maximum (VBM) and the conduction band minimum (CBM) at the Γ point. The VBM mainly consists of p-orbitals of I, and the CBM is composed of p-orbitals of Sn. Thus, the band gap originates from the p−p mixing between Sn and I. Our sX-LDA calculation with SOC yields conduction band dispersion quite different from the previous report,[7] which, we believe, was calculated within the GGA only. The bandwidth of the conduction band increases and suggests a small electron effective mass. The partial hybridization between Sn (s- and p-orbitals) and I (p-orbitals) in the valence band (between −5 and 0 eV) is consistently shown in both studies.

Figure 6c,d shows the band structure and PDOS of yellow $CsSnI_3$ (Y), respectively. The indirect band gap of 2.46 eV is between the X point and the middle of the Γ and Y points. However, the direct band gap (about 2.53 eV) is located at the nearly flat band along Γ to X, which is only 0.07 eV larger than the indirect band gap. This should give rise to a sharp increase in the intensity of the optical transition near the band edge, while the optical transition of the indirect gap is expected to be relatively small. Thus, the calculated direct band gap shows better agreement with the experimental value of 2.55 eV. The overall composition of the PDOS is similar to that of the B-γ phase (Figure 6b,d). The band gap of the Y phase also originates from the hybridization between the p-orbitals of Sn and I. Unlike the case of the B-γ phase, the PDOS of the Y phase shows two kinds of I atoms in yellow $CsSnI_3$. For I(1) and I(2), the hybridization of I p-orbitals with Sn s-orbitals at the top of the valence band and Sn p-orbitals at the bottom of conduction band is more enhanced, whereas I(3) has more lone-pair p-electrons that appear in the middle of the valence band (between −2.5 and −1.0 eV). This difference can be explained by the different local environments of I(1,2) and I(3); I(1) and I(2) are located in the square plane of the octahedron and are bonded to two Sn atoms with a 90° bond angle. On the other hand, the terminal I(3) is bonded to only one Sn atom. The difference in the number of nearest-neighbor atoms accounts for the different electronic structures of I atoms explained above.

The band gap contrast between the B-γ and Y phases is mainly caused by major structural difference between the two phases. As shown in Figure 1, the 3D network of octahedra in the perovskite structure is changed to a pseudo-1D structure built of edge-sharing octahedra chains. The lower dimensionality in the Y phase gives rise to narrower bandwidths (see Figure 6), which leads to an increase in the optical band gap. It is important to note that the total energy of the latter is 0.15 eV per formula unit lower than that of the B-γ phase, indicating the stability of the Y phase over the B-γ phase.

In order to explain the extremely large value of the coefficient of thermal expansion of B-γ phase, we calculated the bulk modulus (B). It represents the resistance of material to uniform compression, defined by eq 2:

$$B = -V\frac{\partial P}{\partial V} \tag{2}$$

where P is pressure and V is volume. The bulk modulus is calculated by fitting calculated total energies in various volumes with the Birch−Murnaghan equation of state.[31] The obtained bulk modulus of B-γ phase is 19.84 GPa. This value is extremely small considering those of other crystalline solid materials: 70 GPa for BeTe,[32] and 322 GPa for TiN[33] and liquid Hg (25.3 GPa). Note that perovskite $CsPbI_3$ that is isostructural to black $CsSnI_3$ shows 23 GPa.[34] Since the bulk modulus is inversely proportional to the coefficient of volumetric thermal expansion via the Gruneisen constant, the obtained bulk modulus supports the extremely large value of the coefficient of thermal expansion of B-γ phase.

Defect Formation Energy. To better understand the p-type nature and unusual observations in transport and optical properties of black $CsSnI_3$, we calculated the defect formation energy. We regarded point defects, a Sn vacancy (V_{Sn}), a Cs vacancy (V_{Cs}), and Sn replacing I (Sn_I), as possible intrinsic p-type sources. We also considered the defect formation energy of an I vacancy (V_I) that might act as an *n*-type source since it can compensate for the hole carrier. Figure 6e shows the defect formation energies of V_{Cs}, V_{Sn}, Sn_I, and V_I as a function of the Fermi level under three different growth conditions: (Sn-poor, I-rich), (Cs-poor, I-rich), and (Sn-rich, I-poor). Under the three growth conditions, the defect formation energy of V_{Sn} generating hole is lower than those of any other defects, which means that V_{Sn} is the most favorable intrinsic defect. The possible compensation of hole by V_I is unfavorable due to its higher formation energy. These results strongly indicate that a major p-type carrier source is V_{Sn}, and the black compound is a nearly intrinsic p-type semiconductor. The facile generation of Sn vacancies would be even better activated by heat energy, resulting in continuously rising electrical conductivity and PL intensities of black $CsSnI_3$. Considering observations of the close correlation of PL and charge transport behavior, coupled with DFT results, the observed near band gap PL plausibly originates from defect centers made by a Sn vacancy, rather than a transition between the band edges.

■ CONCLUSION

We elucidated what drives the facile phase transitions of $CsSnI_3$, whose understanding has been elusive. A surprising finding is that two distinct polymorphs that are stabilized at room temperature readily convert to each other by heating or exposure to air, despite involvement of significant structural reconstruction. One of them is a highly conducting p-type semiconductor and black in color, in contrast to its yellow counterpart with an indirect band gap. They show a dramatic optical band gap difference of 1.25 eV. Their phase transition is derived from stabilization of rattling Cs atoms in the oversized perovskite cages. Therefore, it is controllable by introducing other congeners or more covalent Ag, Cu, or Tl atoms that should better interact with the cages or organic cations for alkali metals.

In going from one perovskite phase form to the next at lower temperature and ultimately to the yellow phase, the density gradually increases as better structural packing is achieved; the yellow phase gains 7−10% in density compared to the other phases. $CsSnI_3$ is a rare case of a material that combines high electrical conductivity and strong PL. Electrical conductivity and thermopower measurements indicate black $CsSnI_3$ to be a

p-type metal, despite the obvious optical band gap of 1.3 eV. Very unusually, it becomes more conducting by heating treatment, which is coupled with the enhancement of near-IR PL at room temperature. These observations possibly result from the readily changing Sn vacancy centers in the structure according to our *ab initio* first-principles DFT calculations. They also suggest that PL originates from the Sn defect centers rather than electron transfer between conduction and valence bands. The ability of $CsSnI_3$ to emit strong near-IR PL at room temperature is a rare property and also important since it is free of rare-earth metals. This study opens up opportunities to discover visible and IR light-emitting materials at room temperature, which is highly desirable in achieving breakthrough applications in photovoltaics,[35] various radiation detectors, and light-emitting diodes because the perovskite structure can incorporate a very broad range of elements.

■ ASSOCIATED CONTENT

Ⓢ Supporting Information

Fractional atomic coordinates, displacement parameters and selected bond distances and angles for $CsSnI_3$ polymorphs; diagrams of volumetric thermal expansion and DTA. This material is available free of charge via the Internet at http://pubs.acs.org.

■ AUTHOR INFORMATION

Corresponding Author

m-kanatzidis@northwestern.edu

Notes

The authors declare no competing financial interest.

[⊥]Deceased

■ ACKNOWLEDGMENTS

This paper is dedicated to the memory of Jung-Hwan Song. Financial support was provided by the National Science Foundation (Grant DMR-1104965). Use of the Advanced Photon Source was supported by the U.S. Department of Energy, Office of Science, Office of Basic Energy Sciences, under Contract Nos. DE-AC02-06CH11357 and DE-FG02-88ER45372.

■ REFERENCES

(1) Yamada, K.; Funabiki, S.; Horimoto, H.; Matsui, T.; Okuda, T.; Ichiba, S. *Chem. Lett.* **1991**, *20*, 801−804.

(2) Scaife, D. E.; Weller, P. F.; Fisher, W. G. *J. Solid State Chem.* **1974**, *9*, 308−314.

(3) Yamada, K.; Matsui, T.; Tsuritani, T.; Okuda, T. *Z. Naturforsch., A: Phys. Sci.* **1990**, *45*, 307−312.

(4) Shum, K.; Chen, Z.; Qureshi, J.; Yu, C.; Wang, J. J.; Pfenninger, W.; Vockic, N.; Midgley, J.; Kenney, J. T. *Appl. Phys. Lett.* **2010**, *96*, 221903.

(5) Mitzi, D. B.; Wang, S.; Feild, C. A.; Chess, C. A.; Guloy, A. M. *Science* **1995**, *267*, 1473−1476. Mitzi, D. B.; Feild, C. A.; Harrison, W. T. A.; Guloy, A. M. *Nature* **1994**, *369*, 467−469.

(6) Kojima, A.; Teshima, K.; Shirai, Y.; Miyasaka, T. *J. Am. Chem. Soc.* **2009**, *131*, 6050−6051.

(7) Borriello, I.; Cantele, G.; Ninno, D. *Phys. Rev. B* **2008**, *77*, 235214.

(8) Romani, A.; Clementi, C.; Miliani, C.; Favaro, G. *Acc. Chem. Res.* **2010**, *43*, 837−846.

(9) Kuriki, K.; Koike, Y.; Okamoto, Y. *Chem. Rev.* **2002**, *102*, 2347−2356.

(10) Kido, J.; Okamoto, Y. *Chem. Rev.* **2002**, *102*, 2357−2368.

(11) Hemmila, I.; Webb, S. *Drug Discovery Today* **1997**, *2*, 373−381.

(12) Bünzli, J. C. G.; Piguet, C. *Chem. Soc. Rev.* **2005**, *34*, 1048−1077.

(13) Sheldrick, G. M. *Acta Crystallogr. A* **2008**, *64*, 112−122.

(14) (a) Chung, I.; Song, J. H.; Jang, J. I.; Freeman, A. J.; Ketterson, J. B.; Kanatzidis, M. G. *J. Am. Chem. Soc.* **2009**, *131*, 2647−2656. (b) Trikalitis, P. N.; Rangan, K. K.; Bakas, T.; Kanatzidis, M. G. *J. Am. Chem. Soc.* **2002**, *124*, 12255−12260.

(15) Wimmer, E.; Krakauer, H.; Weinert, M.; Freeman, A. J. *Phys. Rev. B* **1981**, *24*, 864−875.

(16) Hedin, L.; Lundqvist, B. I. *J. Phys. C: Solid State Phys.* **1971**, *4*, 2064−2083.

(17) MacDonald, A. H.; Pickett, W. E.; Koelling, D. D. *J. Phys. C* **1980**, *13*, 2675−2683.

(18) Bylander, D. M.; Kleinman, L. *Phys. Rev. B* **1990**, *41*, 7868−7871.

(19) (a) Chung, I.; Biswas, K.; Song, J. H.; Androulakis, J.; Chondroudis, K.; Paraskevopoulos, K. M.; Freeman, A. J.; Kanatzidis, M. G. *Angew. Chem., Int. Ed.* **2011**, *50*, 8834−8838. (b) Chung, I.; Song, J. H.; Kim, M. G.; Malliakas, C. D.; Karst, A. L.; Freeman, A. J.; Weliky, D. P.; Kanatzidis, M. G. *J. Am. Chem. Soc.* **2009**, *131*, 16303−16312. (c) Bera, T. K.; Song, J. H.; Freeman, A. J.; Jang, J. I.; Ketterson, J. B.; Kanatzidis, M. G. *Angew. Chem., Int. Ed.* **2008**, *47*, 7828−7832. (d) Kim, M.; Freeman, A. J.; Geller, C. B. *Phys. Rev. B* **2005**, *72*, 035205.

(20) Van de Walle, C. G.; Neugebauer, J. *J. Appl. Phys.* **2004**, *95*, 3851−3879.

(21) Blochl, P. E. *Phys. Rev. B* **1994**, *50*, 17953−17979.

(22) Kresse, G.; Hafner, J. *Phys. Rev. B* **1993**, *47*, 558−561.

(23) Perdew, J. P.; Burke, K.; Ernzerhof, M. *Phys. Rev. Lett.* **1996**, *77*, 3865−3868.

(24) Mauersberger, P.; Huber, F. *Acta Crystallogr., Sect. B: Struct. Sci* **1980**, *36*, 683−684.

(25) Shannon, R. D. *Acta Crystallogr. A* **1976**, *32*, 751−767.

(26) Thiele, G.; Serr, B. R. *Z. Kristallogr.* **1995**, *210*, 64−64.

(27) Takahashi, Y.; Obara, R.; Lin, Z.-Z.; Takahashi, Y.; Naito, T.; Inabe, T.; Ishibashi, S.; Terakura, K. *Dalton Trans.* **2011**, *40*, 5563−5568.

(28) Tudela, D.; J. Sanchez-Herencia, A.; Diaz, M.; Fernandez-Ruiz, R.; Menendez, N.; D. Tornero, J. *J. Chem. Soc., Dalton Trans.* **1999**, 4019−4023.

(29) Bockris, J. O. M.; Reddy, A. K. N.; Gamboa-Aldeco, M. E. *Modern electrochemistry: Fundamentals of electrodics*, Vol. 2, 2nd ed.; Springer: New York, 2000.

(30) Frangioni, J. V. *Curr. Opin. Chem. Biol.* **2003**, *7*, 626−634.

(31) Birch, F. *Phys. Rev.* **1947**, *71*, 809−824.

(32) González-Díaz, M.; Rodríguez-Hernández, P.; Muñoz, A. *Phys. Rev. B* **1997**, *55*, 14043−14046.

(33) Stampfl, C.; Mannstadt, W.; Asahi, R.; Freeman, A. J. *Phys. Rev. B* **2001**, *63*, 155106.

(34) Chang, Y. H.; Park, C. H.; Matsuishi, K. *J. Korean Phys. Soc.* **2004**, *44*, 889−893.

(35) Chung, I.; Lee, B. H.; He, J.; Chang, R; Kanatzidis, M. G. *Nature* **2012**, DOI: 10.1038/nature11067.